

Signatures of Fermi Arcs in the Quasiparticle Interferences of the Weyl Semimetals TaAs and NbP

Guoqing Chang,^{1,2} Su-Yang Xu,^{3,*} Hao Zheng,³ Chi-Cheng Lee,^{1,2} Shin-Ming Huang,^{1,2} Ilya Belopolski,³
 Daniel S. Sanchez,³ Guang Bian,³ Nasser Alidoust,³ Tay-Rong Chang,⁴ Chuang-Han Hsu,^{1,2}
 Horng-Tay Jeng,^{4,5} Arun Bansil,⁶ Hsin Lin,^{1,2,†} and M. Zahid Hasan^{3,‡}

¹Centre for Advanced 2D Materials and Graphene Research Centre,

National University of Singapore, 6 Science Drive 2, Singapore 117546

²Department of Physics, National University of Singapore, 2 Science Drive 3, Singapore 117542

³Laboratory for Topological Quantum Matter and Spectroscopy (B7), Department of Physics,

Princeton University, Princeton, New Jersey 08544, USA

⁴Department of Physics, National Tsing Hua University, Hsinchu 30013, Taiwan

⁵Institute of Physics, Academia Sinica, Taipei 11529, Taiwan

⁶Department of Physics, Northeastern University, Boston, Massachusetts 02115, USA

(Received 10 November 2015; published 10 February 2016)

The recent discovery of the first Weyl semimetal in TaAs provides the first observation of a Weyl fermion in nature. Such a topological semimetal features a novel type of anomalous surface state, the Fermi arc, which connects a pair of Weyl nodes through the boundary of the crystal. Here, we present theoretical calculations of the quasiparticle interference (QPI) patterns that arise from the surface states including the topological Fermi arcs in the Weyl semimetals TaAs and NbP. Most importantly, we discover that the QPI exhibits termination points that are fingerprints of the Weyl nodes in the interference pattern. Our results, for the first time, propose a universal interference signature of the topological Fermi arcs in TaAs, which is fundamental for scanning tunneling microscope (STM) measurements on this prototypical Weyl semimetal compound. More generally, our work provides critical guideline and methodology for STM studies on new Weyl semimetals. Further, the scattering channels revealed by our QPIs are broadly relevant to surface transport and device applications based on Weyl semimetals.

DOI: 10.1103/PhysRevLett.116.066601

Weyl fermion semimetals are an exciting frontier of condensed matter physics and materials science. Such a crystal hosts Weyl fermionic quasiparticles in the electronic band structure and admits a topological classification beyond band insulators [1]. It has deep analogies with particle physics and leads to unique topological properties [2–9]. Specifically, the Weyl fermions correspond to points of bulk band degeneracy, Weyl nodes. Each Weyl node has a definite chirality or chiral charge, which is a monopole or antimonopole of Berry curvature in momentum space. The chiral charge is associated with an integer-valued topological index. This guarantees a new topological surface state, a Fermi arc, which connects the Weyl nodes through the boundary of the sample. In contrast to topological insulators, both the surface and the bulk of Weyl semimetals can give rise to new physics, opening up wide-ranging research opportunities. In the bulk, a Weyl semimetal crystal paves the way for studying the properties of the elusive Weyl fermionic particle in high energy physics by tabletop experiments. The presence of parallel electrical and magnetic fields can break the apparent conservation of the chiral charge due to the chiral anomaly, making a Weyl semimetal, unlike ordinary nonmagnetic metals, more conductive with an increasing magnetic field

[6,10,11]. Chiral photons can couple differently to Weyl fermions of opposite chiralities, leading to a spontaneous anomalous Hall current [12]. The surface Fermi arcs feature a new type of quantum oscillation in transport, where electrons move in real space between different surfaces of a bulk sample when executing a constant-energy orbit in momentum space under an external magnetic field [7–9]. These phenomena make new physics accessible and suggest potential applications.

The recent discovery of Weyl semimetal TaAs provided the first material realization of this new phase of matter [13–15]. Both the Weyl fermions and the Fermi arcs have been directly observed in TaAs by photoemission experiments [15]. Following the discovery, later ARPES results cemented the Weyl state in TaAs and studied the other three compounds in the same family, namely NbAs, TaP, and NbP [16–27]. On the other hand, scanning tunneling microscopy (STM) experiments had been lacking. In particular, the QPI pattern that arises from Fermi arcs is a very interesting topic that has not been well studied even in theory, except a few works for arcs at topological-superconductor surfaces [28,29]. Only very recently, the first STM study of the Weyl semimetal NbP has been reported [30]. Historically, STM has been proven as a very

powerful tool in the fields of high T_c superconductors, graphene, and topological insulators due to its simultaneous spatial, energy, and (quasi-) momentum resolution [31–35]. Moreover, the QPI reveals the scattering processes of the surface electrons by defects, which cannot be directly obtained from ARPES measurements. The scattering processes are fundamental in understanding the transport properties because electrical transport (e.g., resistivity) signals arise from scatterings of the electrons at the Fermi level by defects at low temperatures. In the case of Weyl semimetals, the surface electrons are Fermi arcs. Hence, our QPI results are broadly relevant to surface transport and device applications based on Weyl semimetals.

In this Letter, we theoretically compute the quasiparticle interference patterns (QPIs) that arise from the surface states of the Weyl semimetals TaAs and NbP, including the topological Fermi arcs. Our results answer the following important questions: (i) What is the configuration of the QPI? (ii) What are the scattering channels that lead to the observed dominant features in the QPI? (iii) Is there any feature associated with the topological Fermi arcs? (iv) Is there any feature associated with the Weyl nodes, i.e., the k space locations where the Fermi arcs are terminated? In general, our results provide crucial theoretical information for any future STM studies on Weyl semimetals. Moreover, the scattering channels theoretically uncovered here have important implications for surface transport of Weyl semimetals.

We conducted first-principles band structure calculations of TaAs and NbP within the framework of the density functional theory (DFT) using the generalized gradient approximation (GGA) [36]. Spin-orbit coupling was included in the self-consistency cycles. The Wannier functions of TaAs (NbP) for the Ta (Nb) s and d and the As (P) p orbitals were generated [37]. By combining the bulk Wannier functions and the surface part of slab Wannier functions, we calculated the surface spectral weight of a semi-infinite (001) slab using the iterative Green's function method. We then calculated the QPIs based on the surface Green's function using the T -matrix approach [35]. The main equations governing the QPI could be written as

$$\text{QPI}(\mathbf{q}, \omega) = \frac{i}{2\pi} \int \frac{d^2\mathbf{k}}{(2\pi)^2} [B(\mathbf{q}, \omega) - B^*(\mathbf{q}, \omega)], \quad (1)$$

$$B(\mathbf{q}, \omega) = \text{Tr}[G(\mathbf{k}, \omega)T(\mathbf{k}, \omega)G(\mathbf{k} + \mathbf{q}, \omega)], \quad (2)$$

where \mathbf{q} is the scattering vector, ω is the energy, G is the surface Green's function, and T contains the matrix element effects of impurity. T takes the form,

$$T(\mathbf{k}, \omega) = \left[1 - V_{\text{impurity}} \int \frac{d^2\mathbf{k}}{(2\pi)^2} G(\mathbf{k}, \omega) \right]^{-1} V_{\text{impurity}}, \quad (3)$$

where V_{impurity} is the impurity potential. In order to choose a reasonable T that qualitatively captures the real scenario in experiments, we compared our QPI calculations with our STM QPI data on NbP [30]. From our STM data [30], we

discovered that the scatterings between two states of different orbitals or opposite spins were strongly suppressed. This agreed with the fact that the impurities were nonmagnetic and suggested that the impurities were nearly isotropic. Guided by this experimental finding, we used $T = 1$, which disallowed scatterings between states of opposite spins or different orbitals. We believe that the above constructions capture the dominant features in the STM experiments, which has been proven in our STM work on NbP [30]. More detailed descriptions of the calculation methods and the QPI using a T matrix allowing interorbital scatterings are presented in the Supplemental Material [38].

Figure 1(a) shows the theoretical calculated As-terminated (001) surface Fermi surface of TaAs (001). We consider the pnictide termination throughout this work as it is the natural cleavage found in all experiments [16–27,30]. The calculated surface state Fermi surface is in excellent agreement with our ARPES data on TaAs [15]. We identify three prominent features, namely, an elliptical feature at the \bar{X} point, a bowtie shaped feature at the \bar{Y} points, and a crescent-shaped feature near the midpoint of the $\bar{\Gamma} - \bar{X}$ or $\bar{\Gamma} - \bar{Y}$ line. Because of the close proximity of the Weyl nodes near the \bar{X} (\bar{Y}) point, the corresponding Fermi arc is extremely short and hence does not have any observable effects to the QPI pattern. On the other hand, the crescent feature consists of

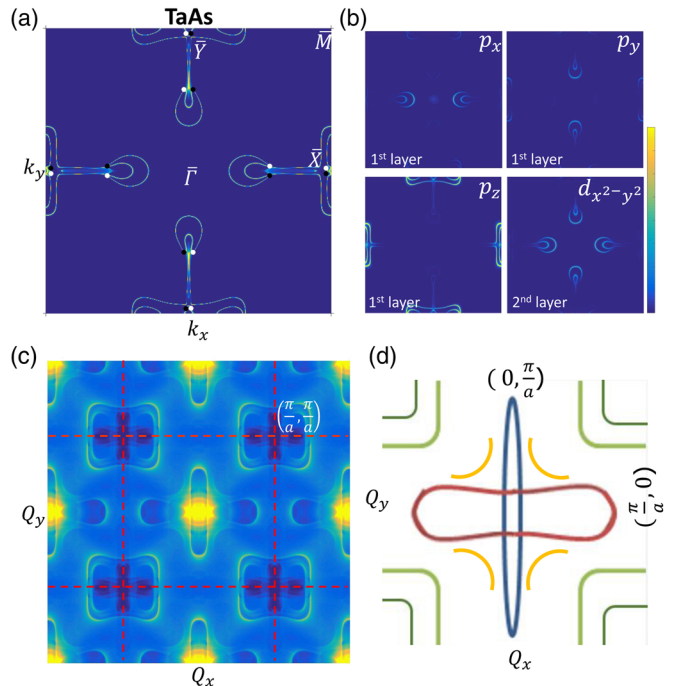


FIG. 1. Theoretically calculated surface Fermi surface and QPI pattern on the TaAs(001) surface. (a) Calculated (001) surface Fermi surface of TaAs. The black and white dots indicate the projected Weyl nodes with positive and negative chiral charges. (b) Electronic states on the Fermi surface that arise from different orbitals. The first layer is As whereas the second layer is Ta. (c) Calculated QPI pattern based on the Fermi surface in panel (a). (d) A sketch of the QPI pattern that corresponds to the real calculation in panel (c).

Fermi arcs that join each other at the two end points, which correspond to projected Weyl nodes with projected chiral charge of ± 2 . We further study the orbital characters of the crescent Fermi arcs. As shown in Fig. 1(b), the crescent Fermi arcs arise from the p_x and p_y orbitals from the first layer, the As atoms, and $d_{x^2-y^2}$ orbital from the second layer, the Ta atoms. The calculated QPI pattern in Fig. 1(c) shows a rich structure, indicating that the scattering behavior on the TaAs surface is complicated. We sketch the dominant features in Fig. 1(d). Near the origin of the QPI image, we find an elliptical contour and a bowtie-shaped contour, whose long axes are perpendicular to each other. At each corner of the QPI, we observe two concentric squares. In addition, we also find weak features that seem to be open curves in each quadrant, as noted by the yellow curves.

We study the scattering channel for the dominant features in the QPI. In Fig. 2, we only consider the bowtie-shaped and elliptical features at the surface Brillouin zone (BZ)

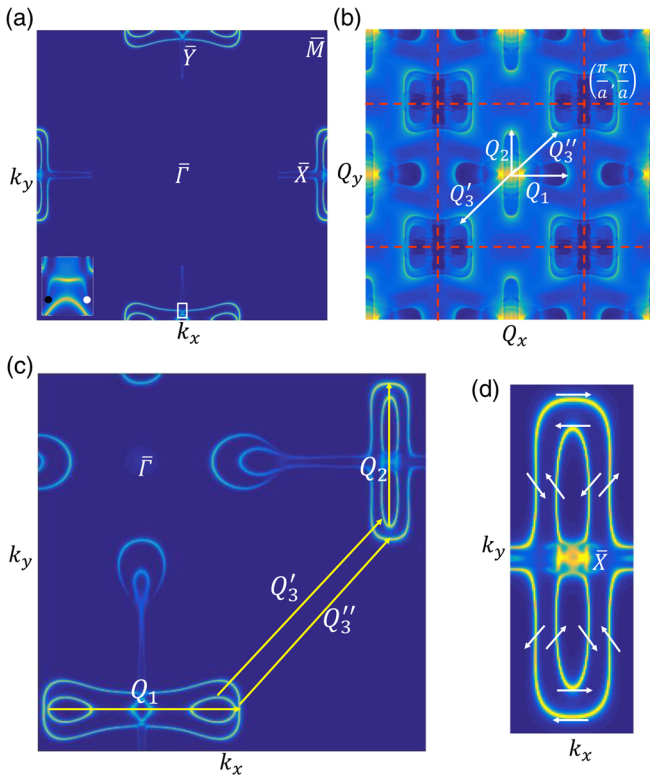


FIG. 2. Quasiparticle scattering that arises from trivial surface states. (a) Calculated surface Fermi surface where the crescent shaped Fermi arcs are manually removed. The inset shows a zoomed-in view of the k space region highlighted by the white box, which encloses a pair of Weyl nodes near the surface BZ boundary \bar{Y} point. It can be seen that the Fermi arc is a very short line that directly connects the pair of nodes. Since the pair of nodes are too close to each other, the Fermi arc does not have any significant impact to the calculated QPI pattern. (b) Theoretical QPI pattern based on the Fermi surface in panel (a). Four characteristic scattering vectors (Q_1 , Q_2 , Q'_3 , and Q''_3) are shown. (c) The four scattering vectors (Q_1 , Q_2 , Q'_3 , and Q''_3) in k space. (d) A sketch of the spin texture of the elliptical surface Fermi contours at the \bar{X} point.

boundaries by manually removing the crescent-shaped Fermi arcs from the Fermi surface. The Fermi arcs near the BZ boundaries are too short to have any real impact. The calculated QPI pattern based on this modified Fermi surface is shown in Fig. 2(b), where almost all dominant features in the full pattern in Fig. 1(c) are reproduced except the weak features noted by the yellow curves in Fig. 1(d). In order to understand the origin of these QPI features, we consider possible scattering channels of the Fermi surface. We consider the following scattering vectors, Q_1 , Q_2 , Q'_3 , and Q''_3 , as shown in Fig. 2(b). By comparing the vector lengths in k space and in Q space, one can figure out the scattering channels. From Fig. 2(c), we clearly resolve that Q_1 and Q_2 are intracontour scattering within a bowtie-shaped or an elliptical feature in the Fermi surface, while Q'_3 and Q''_3 are the intercontour scattering between a bowtie-shaped feature and an elliptical feature. More importantly, the elliptical and bowtie shaped features in the Fermi surface (k space) and in the QPI pattern (Q space) have almost identical line shapes. This similarity makes the identification of the QPI feature quite straightforward and reliable. In addition, one may notice that the elliptical feature in the Fermi surface (k space) consists of two concentric contours at each \bar{X} point but the resulting elliptical feature in the QPI (Q space) is only onefold. This is due to the fact that the elliptical feature in the Fermi surface is located at the \bar{X} point, which is a time-reversal invariant Kramers' point. Hence, the spin texture [Fig. 2(d)] requires that the scattering can only occur in between the inner and the outer elliptical contour.

We now study the QPI features that arise from the crescent Fermi arcs. We note that on the top layer (As atoms), the crescent arcs along $\bar{\Gamma} - \bar{X}$ arise from the p_x orbital whereas those $\bar{\Gamma} - \bar{Y}$ arise from the p_y orbital [Fig. 1(b)]. Hence, if one only considers the top layer, the scattering between the crescent Fermi arcs would be nearly suppressed. In other words, in order to observe the crescent Fermi arcs in the QPI, signals from the second (Ta) layer have to be significant in the STM data. As shown in Fig. 3(b), we find a complicated feature near the center of each quadrant in Q space. This feature is due to the scattering between the crescent Fermi arcs along $\bar{\Gamma} - \bar{X}$ and those along $\bar{\Gamma} - \bar{Y}$, as noted by the scattering vectors Q_4 to Q_7 . The zoomed-in view in Fig. 3(d) shows that it consists of four nonclosed curves that join each other at four termination points. We sketch a schematic for this feature in Fig. 4(b). Among the four curves in Fig. 4(b), the red curve is closest to the Q space origin, meaning that it has the shortest Q vector. Therefore, the red curve corresponds to the scattering between the two outer arcs as noted by the red arrow in Fig. 4(a). Similarly, one can understand the other three curves. Specifically, the black, orange, and purple curves come from the scatterings between the two inner arcs, between the outer ($O1$) and the inner ($I2$) arcs, and between the outer ($O2$) and the inner ($I1$) arcs, respectively. We now consider the meaning of these termination points, where the four curves join each other in the QPI. As shown in Fig. 4(a), we start by considering the scattering from the outer ($O1$) arc to the outer ($O2$) arc noted

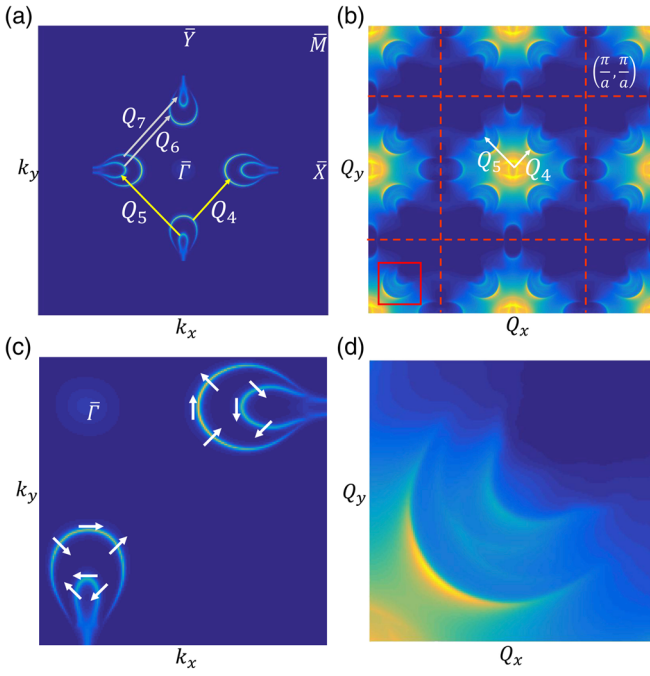


FIG. 3. Quasiparticle scattering that arises from the topological Fermi arcs. (a) Calculated surface Fermi surface containing only the crescent Fermi arcs. (b) Theoretical QPI pattern based on panel (a). (c) A sketch of the spin texture of the crescent Fermi arcs. (d) A close-up view of the complex QPI feature that arise from the crescent Fermi arcs in one quadrant in Q space.

by the red arrow; we move the ending point of the arrow through a Weyl node (the black dot) onto the inner (I_2) arc; through this movement, the red arrow evolves into the orange arrow. Therefore, we see that the termination point in Fig. 4(b) is a fingerprint of the Weyl node in the QPI pattern because it corresponds to the scattering from a state on the outer (O_1) arc to the Weyl node noted by the black dot [Fig. 4(a)]. By the same token, it is straightforward to figure out that the other three termination points in Fig. 4(b) are fingerprints of the other three Weyl nodes in Fig. 4(a). While the ending point of the scatterings are the Weyl nodes, the starting points are more subtle. In the Supplemental Material [38], we show that starting state is determined by a complex consideration of both the joint density of states (JDOS) and the spin selection rule.

The QPI of the NbP surface states is also shown in the Supplemental Material [38]. We find that the dominant features in NbP's QPI pattern is qualitatively the same as that of TaAs when the same T matrix is used. The only difference is that the features from the crescent Fermi arcs are too weak to be resolved in our calculation. The calculated QPI patterns of NbP are consistent with our STM data on NbP reported in Ref. [30].

In the Supplemental Material [38], we have further investigated the QPI patterns that arise from a different form impurity potential, which allows interorbital scatterings. QPIs from interorbital scatterings may become visible in real experiments if the anisotropy of the impurity potential is significant.

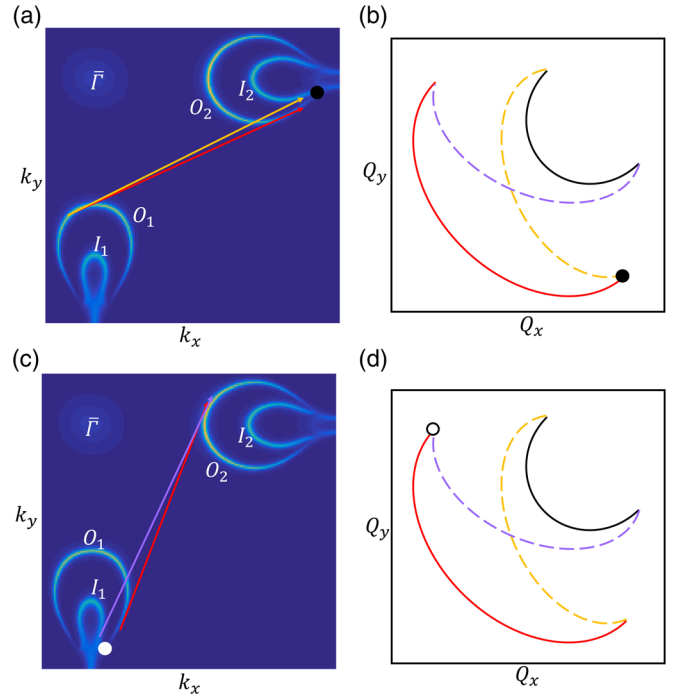


FIG. 4. Fingerprints of the Weyl nodes in the interference pattern. (a) Calculated surface Fermi surface containing a pair of crescent Fermi arcs along $\bar{\Gamma} - \bar{X}$ and another pair along $\bar{\Gamma} - \bar{Y}$. The scattering vectors from outer (O_1) arc to outer (O_2) arc is noted by the red arrow. Scattering vectors from outer (O_1) arc to inner (I_2) arc is noted by the orange arrow. The Weyl nodes near the $\bar{\Gamma} - \bar{X}$ axis are noted by a black dot. (b) Schematic illustration of the QPI pattern based on the Fermi surface in panel (a). The red, orange, purple, and black curves correspond to the scattering between the outer (O_1) and outer (O_2) arcs, between outer (O_1) and inner (I_2) arcs, between inner (I_1) and outer (O_2) arcs, and between inner (I_1) and inner (I_2) arcs, respectively. (c),(d) Same as panels (a),(b), the only difference is that we consider the different scattering vectors.

We compare the STM signature of Fermi arcs presented here with that we obtained in angle-resolved photoemission spectroscopy (ARPES) [15,20,23]. In ARPES, one can show the existence of Fermi arcs without relying on the details of theoretical calculations. Specifically, this can be done by counting the net number of chiral edge modes along a closed k loop that encloses a Weyl node in the surface electronic band structure in ARPES, as systematically discussed in Refs. [15,20,23]. By contrast, what we found out here is that although the calculated QPI pattern shows fingerprints of the Fermi arcs and Weyl nodes, this is only achieved by referencing the theoretical calculation. This is due to the indirect nature of STM measurements as it measures the momentum transfer rather than the real momentum, which is true in all QPI studies on many different materials including graphene and topological insulators [31–35]. Although being indirect, the QPI patterns calculated here propose another evidence that is independent from the ARPES demonstrations [15,20,23], which is important for this rapidly developing field.

Moreover, the QPI reveals the scattering processes of the surface electrons by defects, which cannot be directly obtained from ARPES measurements. Hence, our QPI results are broadly relevant to surface transport and device applications based on Weyl semimetals.

Work at Princeton University was supported by the National Science Foundation, Division of Materials Research, under the Grant No. NSF-DMR-1507585. Work at the National University of Singapore was supported by the National Research Foundation (NRF), Prime Minister's Office, Singapore, under its NRF fellowship (NRF Grant No. NRF-NRFF2013-03). T.-R. C. and H.-T. J. were supported by the National Science Council, Taiwan. H.-T. J. also thanks the National Center for High-Performance Computing, Computer and Information Network Center National Taiwan University, and National Center for Theoretical Sciences, Taiwan, for technical support. Work at Northeastern University was supported by the U.S. DOE/BES Grant No. DE-FG02-07ER46352, and benefited from Northeastern University's Advanced Scientific Computation Center (ASCC) and the National Energy Research Scientific Computing Center under the DOE Grant No. DE-AC02-05CH11231. G. C., S. M. H., T. R. C, and H. L.'s visits to Princeton University were partially funded by the Gordon and Betty Moore Foundations Emergent Phenomena in Quantum Systems Initiative under the Grant No. GBMF4547 (M. Z. H.).

G. C., S-Y. X., and H. Z. contributed equally to this work.

^{*}Corresponding author.

suyangxu@princeton.edu

[†]Corresponding author.

nilihish@gmail.com

[‡]Corresponding author.

mzhasan@princeton.edu

- [1] A. M. Turner and A. Vishwanath, arXiv:1301.0330.
- [2] H. Weyl, *I. Z. Phys.* **56**, 330 (1929).
- [3] L. Balents, *Physics* **4**, 36 (2011).
- [4] X. Wan, A. M. Turner, A. Vishwanath, and S. Y. Savrasov, *Phys. Rev. B* **83**, 205101 (2011).
- [5] A. A. Burkov and L. Balents, *Phys. Rev. Lett.* **107**, 127205 (2011).
- [6] H. B. Nielsen and M. Ninomiya, *Phys. Lett. B* **130**, 389 (1983)
- [7] T. Ojanen, *Phys. Rev. B* **87**, 245112 (2013).
- [8] P. Hosur, *Phys. Rev. B* **86**, 195102 (2012).
- [9] A. C. Potter, I. Kimchi, and A. Vishwanath, *Nat. Commun.* **5**, 5161 (2014).
- [10] C. Zhang *et al.*, arXiv:1503.02630.
- [11] X. Huang, L. Zhao, Y. Long, P. Wang, D. Chen, Z. Yang, H. Liang, M. Xue, H. Weng, Z. Fang, X. Dai, and G. Chen, *Phys. Rev. X* **5**, 031023 (2015).
- [12] C.-K. Chan, P. A. Lee, K. S. Burch, J. H. Han, and Y. Ran, *Phys. Rev. Lett.* **116**, 026805 (2016).
- [13] S.-M. Huang, S.-Y. Xu, I. Belopolski, C.-C. Lee, G. Chang, B. Wang, N. Alidoust, G. Bian, M. Neupane, C. Zhang, S.

Jia, A. Bansil, H. Lin, and M. Z. Hasan, *Nat. Commun.* **6**, 7373 (2015).

- [14] H. Weng, C. Fang, Z. Fang, B. A. Bernevig, and X. Dai, *Phys. Rev. X* **5**, 011029 (2015).
- [15] S.-Y. Xu, I. Belopolski, N. Alidoust, M. Neupane, G. Bian, C. Zhang, R. Sankar, G. Chang, Z. Yuan, C.-C. Lee, S.-M. Huang, H. Zheng, J. Ma, D. S. Sanchez, B. Wang, A. Bansil, F. Chou, P. P. Shibayev, H. Lin, S. Jia, and M. Z. Hasan, *Science* **349**, 613 (2015).
- [16] B. Q. Lv, H. M. Weng, B. B. Fu, X. P. Wang, H. Miao, J. Ma, P. Richard, X. C. Huang, L. X. Zhao, G. F. Chen, Z. Fang, X. Dai, T. Qian, and H. Ding, *Phys. Rev. X* **5**, 031013 (2015).
- [17] B. Q. Lv, N. Xu, H. M. Weng, J. Z. Ma, P. Richard, X. C. Huang, L. X. Zhao, G. F. Chen, C. E. Matt, F. Bisti, V. N. Strocov, J. Mesot, Z. Fang, X. Dai, T. Qian, M. Shi, and H. Ding, *Nat. Phys.* **11**, 724 (2015).
- [18] L. X. Yang, Z. K. Liu, Y. Sun, H. Peng, H. F. Yang, T. Zhang, B. Zhou, Y. Zhang, Y. F. Guo, M. Rahn, D. Prabhakaran, Z. Hussain, S.-K. Mo, C. Felser, B. Yan, and Y. L. Chen, *Nat. Phys.* **11**, 728 (2015).
- [19] S.-Y. Xu *et al.*, *Nat. Phys.* **11**, 748 (2015).
- [20] S.-Y. Xu *et al.*, *Sci. Adv.* **1**, e1501092 (2015).
- [21] N. Xu *et al.*, arXiv:1507.03983.
- [22] Z. K. Liu, L. X. Yang, Y. Sun, T. Zhang, H. Peng, H. F. Yang, C. Chen, Y. Zhang, Y. F. Guo, D. Prabhakaran, M. Schmidt, Z. Hussain, S.-K. Mo, C. Felser, B. Yan, and Y. L. Chen, *Nat. Mater.* **15**, 27 (2016).
- [23] I. Belopolski, S.-Y. Xu, D. Sanchez, G. Chang, C. Guo, M. Neupane, H. Zheng, C.-C. Lee, S.-M. Huang, G. Bian, N. Alidoust, T.-R. Chang, B. Wang, X. Zhang, A. Bansil, H.-T. Jeng, H. Lin, S. Jia, and M. Z. Hasan, *Phys. Rev. Lett.* **116**, 066802 (2016).
- [24] D. F. Xu, Y. P. Du, Z. Wang, Y. P. Li, X. H. Niu, Q. Yao, P. Dudin, Z.-A. Xu, X. G. Wan, and D. L. Feng, *Chin. Phys. Lett.* **32**, 107101 (2015).
- [25] S. Souma, Z. Wang, H. Kotaka, T. Sato, K. Nakayama, Y. Tanaka, H. Kimizuka, T. Takahashi, K. Yamauchi, T. Oguchi, K. Segawa, and Y. Ando, arXiv:1510.01503.
- [26] S.-Y. Xu *et al.*, arXiv:1510.08430.
- [27] B. Q. Lv, S. Muff, T. Qian, Z. D. Song, S. M. Nie, N. Xu, P. Richard, C. E. Matt, N. C. Plumb, L. X. Zhao, G. F. Chen, Z. Fang, X. Dai, J. H. Dil, J. Mesot, M. Shi, H. M. Weng, and H. Ding, *Phys. Rev. Lett.* **115**, 217601 (2015).
- [28] J. D. Sau and S. Tewari, *Phys. Rev. B* **86**, 104509 (2012).
- [29] J. S. Hofmann, R. Queiroz, and A. P. Schnyder, *Phys. Rev. B* **88**, 134505 (2013).
- [30] H. Zheng *et al.*, *ACS Nano* **10**, 1378 (2016).
- [31] J. E. Hoffman, K. McElroy, D.-H. Lee, K. M. Lang, H. Eisaki, S. Uchida, and J. C. Davis, *Science* **297**, 1148 (2002).
- [32] G. M. Rutter, J. N. Crain, N. P. Guisinger, T. Li, P. N. First, and J. A. Stroscio, *Science* **317**, 219 (2007).
- [33] P. Roushan, J. Seo, C. V. Parker, Y. S. Hor, D. Hsieh, D. Qian, A. Richardella, M. Z. Hasan, R. J. Cava, and A. Yazdani, *Nature (London)* **460**, 1106 (2009).
- [34] T. Zhang, P. Cheng, X. Chen, J.-F. Jia, X. Ma, K. He, L. Wang, H. Zhang, X. Dai, Z. Fang, X. Xie, and Q.-K. Xue, *Phys. Rev. Lett.* **103**, 266803 (2009).
- [35] I. Zeljkovic, Y. Okada, C.-Y. Huang, R. Sankar, D. Walkup, W. Zhou, M. Serbyn, F. Chou, W.-F. Tsai, H. Lin, A. Bansil,

- L. Fu, M. Z. Hasan, and V. Madhavan, *Nat. Phys.* **10**, 572 (2014).
- [36] J. P. Perdew, K. Burke, and M. Ernzerhof, *Phys. Rev. Lett.* **77**, 3865 (1996).
- [37] N. Marzari and D. Vanderbilt, *Phys. Rev. B* **56**, 12847 (1997).
- [38] See Supplemental Material at <http://link.aps.org/supplemental/10.1103/PhysRevLett.116.066601> for further details, which is included in Refs. [30,35–37,39,40].
- [39] T. Ozaki, *Phys. Rev. B* **67**, 155108 (2003).
- [40] G. Kresse and J. Hafner, *Phys. Rev. B* **48**, 13115 (1993).